Surface analysis of Roman Sarcophagus using multispectral close-range photogrammetry

Berna Pamuk [1], **Ozgun Akcay [*2]**

¹Çanakkale Onsekiz Mart University, School of Graduate Studies, Department of Geomatics Engineering, Çanakkale, Türkiye
²Çanakkale Onsekiz Mart University, Faculty of Engineering, Department of Geomatics Engineering, Çanakkale, Türkiye

Abstract

Currently, cameras equipped with multispectral sensors are utilized to monitor cultural heritage. However, these cameras have a lower resolution compared to RGB cameras, resulting in a loss of detail during analysis. The method proposed in this study outlines a series of image processing and data analysis techniques for orthophotos generated through the photogrammetric evaluation of images captured with RGB and multispectral cameras. This study first enhances the low-resolution multispectral orthophotos and creates a multispectral image stack. The resulting image stack undergoes dimensional reduction via principal component analysis, followed by the implementation of a clustering algorithm. Consequently, a map is generated to identify and examine surface details using multispectral data. The discrimination capability was verified comparatively by analyzing the histograms of selected subregions from the generated maps. This validation demonstrates that meaningful information is successfully produced from the image stacks. This method offers a rapid, efficient, and adaptable analysis of photogrammetric products necessary for the field of cultural heritage.

1. Introduction

Digital photogrammetric techniques are essential in detecting, examining, preserving, documenting, and presenting archaeological findings and cultural heritage artifacts. Photogrammetry has been discussed and utilized in numerous scientific studies for the rapid and geometrically precise documentation and monitoring of cultural heritage structures [1-4]. In documenting cultural heritage, photogrammetric models serve as a viable alternative to expensive laser scanners regarding geometric accuracy [5,6]. As seen in [7-9], Unmanned Aerial Vehicle (UAV) technology is also a key factor that enhances the photogrammetric analysis capability of historical buildings. [10] created a three-dimensional model of the Selime Cathedral, an ancient ruin in Cappadocia, utilizing UAV images. Although photogrammetry has been used in these fields for many years, it is still a very current scientific research topic due to the developing sensor technology. In 2022, [11] developed a photogrammetric model that successfully interpreted the pictorial cycle by virtually reconstructing the fresco fragments and validating their consistency from iconographic and art-historical points of view. Another scientific challenge in archaeological

photogrammetry is combining point clouds from various sensors, such as cameras, Terrestrial Laser Scanners (TLS), and Simultaneous Localization and Mapping (SLAM), to conduct a comprehensive analysis [12].

Digital photogrammetry has enabled high geometric and radiometric resolution with the widespread availability of multispectral cameras, laser scanners, and standard Red-Green-Blue (RGB) cameras that can only record visible wavelength radiation. [13] created a comprehensive dataset by integrating terrestrial laser scanning and aerial photogrammetry to document the Mosque of Kurşunlu Complex in Eskişehir thoroughly.

Models produced by close-range photogrammetry are essential data sources for documenting artifacts, but they are also crucial for featured visualizations such as holograms [14]. The enormous amount of data collected has led to initiatives such as the Archaeological Data Service for digital archiving [15].

Using RGB photogrammetry and infrared spectroscopy, [16] identified the content of major elements in wooden coffins, such as hematite, cinnabar, and atacamite. On the other hand, [17] compared RGB orthoimages with NDVIs orthoimages of multispectral cameras to measure the erosion process. The average 3D

error of control points was calculated at 1.5 cm and 3 cm for the RGB and multispectral projects, respectively. In another study, the tomb of the diver is an archeological painted tomb in southern Italy that has been investigated by portable equipment, including imaging diagnostics and compositional spectroscopic techniques for identifying pigments and the conservation state of the original painted surface [18]. The obtained results showed that the Tomb of the Diver could belong to a local artisanal tradition and indicate an expression of the local elite culture of Paestum. [19] explained a constructive workflow that enables the integration of photogrammetric modeling, reflectance transformation imaging, and multispectral imaging to create a single representation of an Egyptian-painted wood sarcophagus. [20] introduced the survey of the late 6th century BC Etruscan anthropoid Sarcophagus. In the study, photogrammetry and laser scanning were used for 3D modeling of the Sarcophagus, and then, a metric comparison between the two models was discussed. [21] combined active and passive sensors capable of recording data in different ranges to characterize different construction materials and the main pathologies of Cultural Heritage elements. The results proved that 3D intensity data of laser scanners can be integrated comprehensively with 2D multispectral images.

[22] acquired three-dimensional data for a rock art documentation application using a lightweight multispectral camera to define motifs of the rock art paintings on a cave. The study results indicated that the lightweight multispectral can be utilized as an alternative to terrestrial laser scanners in obtaining rock art painting data for geometric documentation, as their geometric comparison showed a similar geometric quality. [23] described the 3D survey methodology of the Tomb TT214 at Deir al-Medina, Egypt, to integrate the evidence collected in the past on this tomb with a fresh survey in terms of conservation. [24] presented a radiometric evaluation to determine pathologies in the facades of historical buildings by using multispectral imagery.

Many studies on the analysis of sarcophagi contain historical inscriptions and figures as cultural heritage artifacts. [25] examined an inscribed Roman sarcophagus exhibited in the Troy Museum, Canakkale, Turkey, that also has the figure of a young woman on one side. The study discussed that the sarcophagus could probably be dated to the Hadrian or early Antonine period. The back of another Roman sarcophagus with only the main features of the basic design blocked out and the surface dressed in a coarse point indicates the Roman method of prefabrication for mass production. The back of another Roman sarcophagus with only the main features of the basic design and the surface dressed in a coarse point indicates the Roman method of prefabrication for mass production [26].

[27] produced a 3-dimensional model of the sarcophagus and tomb stele from the Roman period in Aksaray Museum using Agisoft Metashape and Pix4d photogrammetric software. As a result of the study, the software performances were compared with the number of photos, point cloud, and location accuracy. To extract a 3D model of a Roman-era sarcophagus more practically, [28] leveraged a mobile phone camera to collect photogrammetric input data. [29] described figures depicted on the sarcophagus and missing parts of the inscriptions using digital imaging methods, Photogrammetry, and Reflectance Transformation Imaging on a columnar sarcophagus in the ancient city of Termessos, Turkey. [30] produced a 3D model of a late antique marble sarcophagus using photogrammetry and Structured Light Scanning and compared two recording techniques to explain failures in detecting the object's surface.

Close-range photogrammetry can accurately identify archaeological rock reliefs. This method allows for the correct interpretation of the symbols on the surface and their meanings [31]. Additionally, photogrammetric techniques can detect discoloration and surface deterioration on stone surfaces due to exposure to sunlight and water over centuries [32,33]. However, the use of multispectral sensors was ignored in these photogrammetric studies. The aim of this study is to investigate the surface of a Roman sarcophagus using orthophotos produced through photogrammetric evaluation with different wavelength sensors. This inspection is conducted by clustering a single stack generated through image sharpening. Section 2 outlines the workflow and methods applied, while Section 3 details the results obtained. Sections 4 and 5 discuss the findings and present the conclusions, respectively.

2. Method

This study was conducted on a sarcophagus in the inventory of the Troy Museum in Çanakkale, Turkey. The sarcophagus, measuring 104 x 231 x 90 cm, was discovered in the Lapseki district of Çanakkale province and dates back to the Ancient Roman period. The four sides of the sarcophagus are adorned with garlands and grape clusters. The large front side features a Tabula Ansata, which was commonly used in Ancient Rome and provides information about the deceased. The Tabula Ansata includes four lines of Latin inscriptions, along with two lines of inscription on the long side of the sarcophagus. The lid of the sarcophagus, which has a triangular pediment, includes grooves. Images of the sarcophagus were captured using RGB and multispectral cameras. The main features of the cameras used are presented in Table 1.

Table 1. Technical specifications for the sensors of each camera

Cameras	Canon EOSM	Mapir Survey3
Resolution (Mp)	24.1	12
Band specifications (nm)	450 – 495	490
	495 – 570	615
	590 – 620	808

In this study, a new methodology was introduced that combines various techniques, including photogrammetry, image processing, and image classification, to analyze the surface features of the sarcophagus. The workflow diagram summarizing all processes is shown in Figure 1.
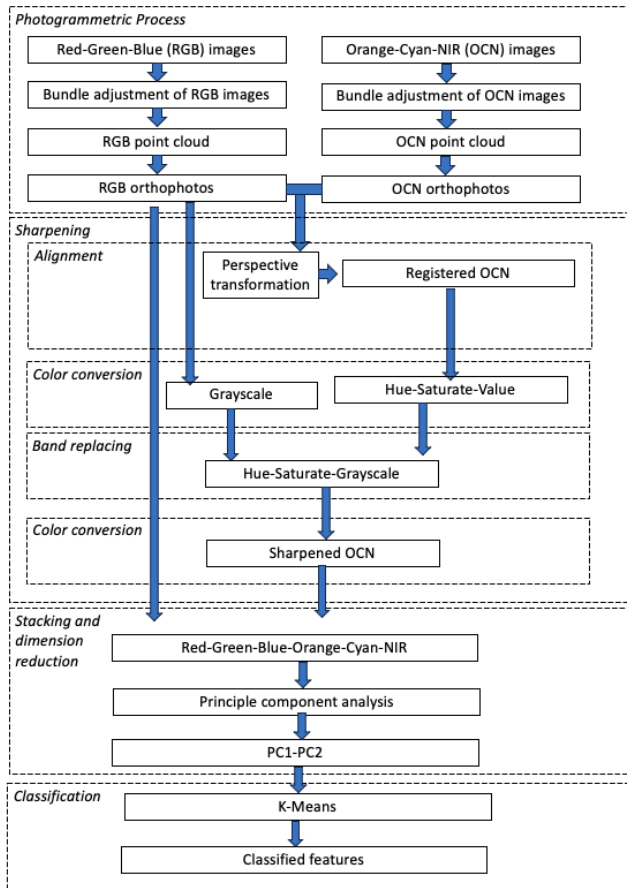
Figure 1. This is the example of figure formatting

Accordingly, the matching, orientation, point cloud, and orthophoto production of RGB and Orange-Cyan-NIR (OCN) images were conducted separately using Agisoft Metashape software. Orthophotos were created by capturing images of one surface of the sarcophagus. This workflow is also applicable to the other three surfaces. Next, the perspective transformation was implemented to evaluate the RGB and OCN orthophotos at the corresponding resolution and pixel coordinate system. Using the 3×3 transformation matrix T, any (X, Y) pixel coordinates of OCN orthophotos can be converted to RGB pixel coordinates (x, y), as indicated in Equations 1 and 2. The transformation matrix T includes parameters a, b, and c related to rotation, scale, and transition, respectively.

$$T = \begin{bmatrix} a_1 & a_2 & b_1 \\ a_3 & a_4 & b_2 \\ c_1 & c_2 & 1 \end{bmatrix} \tag{1}$$

$$\begin{bmatrix} x \\ y \\ 1 \end{bmatrix} = T \begin{bmatrix} X \\ Y \\ 1 \end{bmatrix} \tag{2}$$

Before data fusion, the differences in resolution between two distinct orthophotos are addressed through image sharpening. Panchromatic sharpening techniques specifically designed for satellite imagery enable the enhancement of low-resolution data to match panchromatic band resolution. Notable algorithms include Brovey, Gram-Schmidt, and intensity, hue, and saturation (IHS) methods [34]. In this study, the

algorithmic principles of the IHS method have been modified with practical adjustments. Since this research has no panchromatic band, the high-resolution RGB image is converted into a grayscale single-band image and utilized as a panchromatic image. Conversely, the low-resolution OCN orthophoto image is transformed into IHS format. The V value is substituted with a grayscale high-resolution orthophoto. Finally, the multispectral orthophoto in IHS format with the updated value is converted back to its original three-band image representation format.

After the data was generated as a six-band multispectral stack, the Principal Component Analysis (PCA) dimension reduction method was applied to selected areas of the inscriptions on the surface, allowing representation with fewer than six bands. PCA facilitates compression through linear combinations and new variables to convey meaningful information [35]. In this study, the six-band image stack is reduced to three components to extract the maximum amount of information possible. Finally, the surface features of the sarcophagus were obtained through unsupervised classification. Georeferencing of orthophotos and all post-processing were conducted in a Python environment using the NumPy, OpenCV, and scikit-learn libraries packages.

3. Results

This section presents the results of the intermediate steps in the workflow and provides the final information about the sarcophagus surface.

3.1. Photogrammetric production

Since the two cameras' geometric sensor characteristics, resolution, and lenses differ, the point-matching performance, orientation accuracy, point cloud density, and resolution of the produced orthophotos vary, as shown in Table 2.

Table 2. Technical specifications for the sensors of each

Specifications	Model I	Model II
Input image bands	RGB	OCN
Image size (px)	4000x6000	3000x4000
Number of images	13	18
Number of tie points	11745	13188
Reprojection error (px)	0.839	0.800
Orthophotos size (px)	3318x4455	1765x2333

The px is an abbreviation of the pixel word.

Model I presents the results of the photogrammetric process using the RGB camera, while Model II displays the photogrammetric results generated from OCN camera images. Notably, the output resolution of the RGB camera images is particularly impressive in orthophoto production. Conversely, while OCN camera images demonstrate a certain level of photogrammetric output quality, the information provided by the infrared band, which lies outside the visible spectrum, is significant in this context. It is also observed that the reprojection

errors are quite similar. However, given that the geometric and radiometric pixel quality of the RGB camera is superior, it can be concluded that the RGB photogrammetry results are more reliable.

3.2. Accuracy of the Geometric Alignment

Equation 3 shows the transformation matrix T obtained using four common points selected in each image.

$$T = \begin{bmatrix} 1.849 & 7.0 \times 10^{-2} & 15.222 \\ -0.144 & 1.824 & 191.493 \\ -3.3 \times 10^{-6} & 8.4 \times 10^{-8} & 1.000 \end{bmatrix} \quad (3)$$

The RMSE values in the x and y directions resulting from the transformation are $m_x = \pm 1.35$ px and $m_y = \pm 0.42$ px, respectively. It is observed that the accuracy on the y-axis is relatively high. Conversely, although the error on the x-axis is slightly above 1 pixel, it is sufficiently accurate for the data fusion process to be implemented in the next step.

3.3. Implementation of the Pansharpening

After implementing geometric alignment, a high-resolution single-band grayscale orthophoto, also known as an RGB intensity image with dimensions of 3318x4455, was derived from a three-band RGB orthophoto. Conversely, the low-resolution three-band multispectral orthophoto was transformed into IHS image space. The purpose of producing the high-resolution single-band RGB intensity image is to replace it with the low-resolution intensity channel of the multispectral orthophoto. Consequently, RGB intensity, multispectral hue, and saturation were converted back into RGB space for the pansharpened multispectral orthophoto, as illustrated in Figure 2.
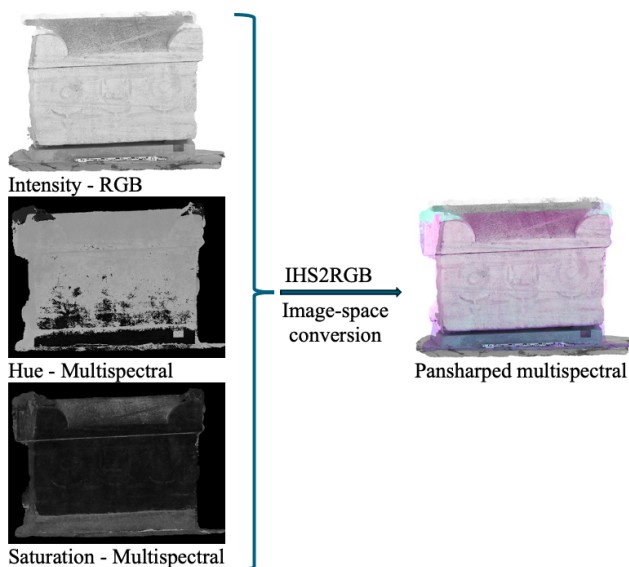

Figure 2. Pansharpening process

3.4. ROIs and Principal Component Analysis

After implementing the pansharpening process, a six-band image stack was created using OCN and RGB orthophotos. As illustrated in Figure 3, regions of interest (ROIs), Region I and Region II, were selected to focus on inspecting the inscriptions and degradations of the sarcophagus surface. The processes implemented separately for the two regions to minimize the impact of local radiometric differences are described in the following sections. Table 3 also presents the average pixel values and their standard deviations of the six-band image stack for each region. The pixel value range for the image bands is from 0 to 255, given that the bit depth is 8. Region II bands with a lower standard deviation than Region I provide a more suitable input for the image classification.

Figure 3. Regions of interests

Table 3. Pixel statistics for Regions I and II

Region	Band	Average pixel value	Standard dev
I	Orange	204.7	20.6
	Cyan	185.3	23.8
	NIR	199.4	20.7
	Red	201.7	23.2
	Green	204.7	21.1
	Blue	206.7	19.0
II	Orange	205.0	11.8
	Cyan	187.0	12.8
	NIR	196.0	11.9
	Red	203.9	13.5
	Green	205.2	12.0
	Blue	204.8	10.9

The number of bands in the image stack can be reduced to better represent visual information with more interpretable and informative content. In this regard, PCA removes highly correlated band information and produces a more streamlined image stack from the multi-band structure. Two separate PCAs were executed for each region, utilizing three components. The explained variance ratios of the two sets of principal components were then obtained, as shown in Table 4. The results indicate that the first principal components (PC1s) of the PCA analysis conducted in Region I and Region II convey information at very high ratios. Consequently, PC1 and PC2 were selected as the two

features for unsupervised classification, while PC3 was excluded due to its low explained variance ratio.

Table 4. The explained variance ratios of the PCA analyses for Regions I and II

Region	PC1	PC2	PC3
I	0.95	0.03	0.01
II	0.96	0.02	0.02

3.5. Clustering

Information extraction was accomplished using a standard K-Means clustering algorithm. The K-means algorithm randomly selects several k centroids and then assigns data points to the nearest cluster by measuring the distance between the cluster center and the data point. The algorithm iteratively optimizes cluster centroids to minimize the sum of squared errors for each k cluster [36].

To determine the optimal number of clusters, inertia values were calculated for 15 clusters and compared separately for Regions I and II, as shown in Figures 4 and 5.
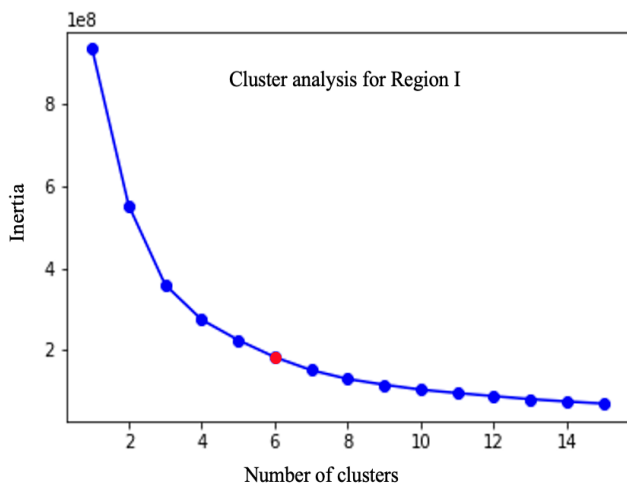

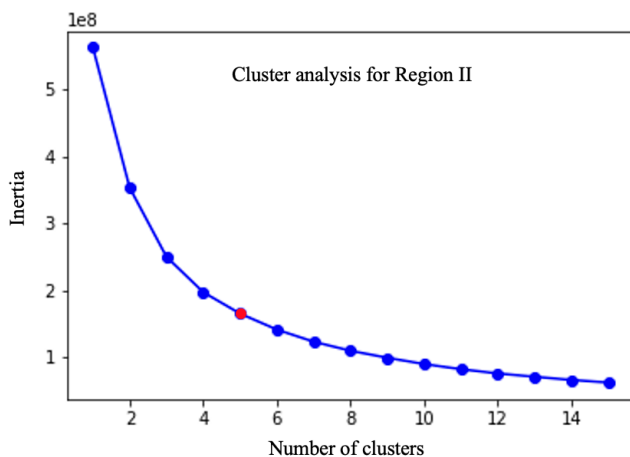**Figure 4.** Definition of the optimal number of clusters for Region I

Figure 5. Definition of the optimal number of clusters for Region II

The optimum cluster number was defined at the point where the graph line forms an elbow, with the selected optimum cluster numbers marked by red dots in the figures. A 6-cluster model with an inertia value of 1.84×10^{-8} was identified as optimal for Region I, while the 5-cluster model with an inertia value of 1.65×10^{-8} was chosen as optimal.

Figures 6 and 7 illustrate the visual discrimination graphs derived from the classifications of the identified cluster numbers based on the principal components.
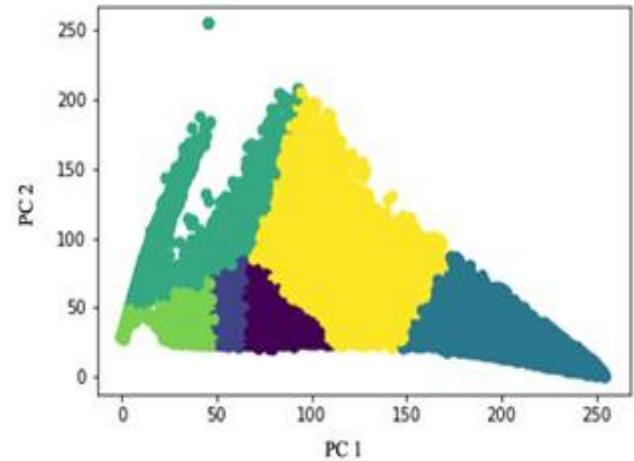

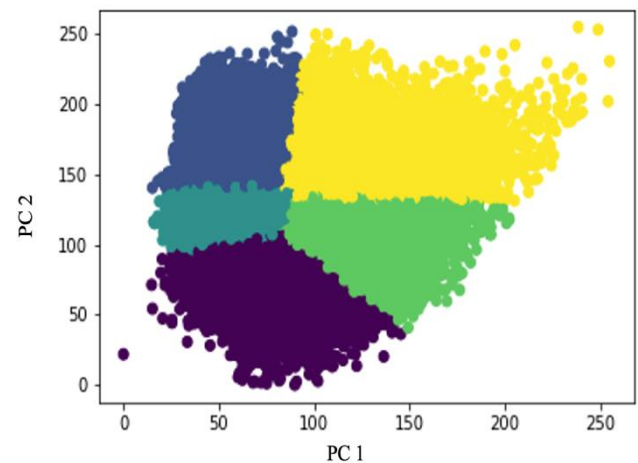**Figure 6.** Cluster allocations of pixels for Region I

Figure 7. Cluster allocations of pixels for Region II

A thematic map was created by projecting the classification results based on pixel values and their locations for visualization. Figures 8 and 9 display the classification maps for Region I and Region II, respectively. It is important to note that the coloring of the maps displayed in Figures 8 and 9 is determined randomly in both clustering, resulting in a lack of color uniformity between the two images.

Figure 8. Visualization of clustering for Region I

Figure 9. Visualization of clustering for Region II

3.6. Validation

To verify the clustering results, histograms were generated for the subregions selected from the two regions and extracted to evaluate the discrimination capability for information extraction. As shown in Figures 10 and 11, a total of six subregions were selected: four subregions in Region I and two subregions in Region II. In addition to the clustering images of these regions, hue, saturation, PC1, RGB, and 3D point cloud depth images are also presented.
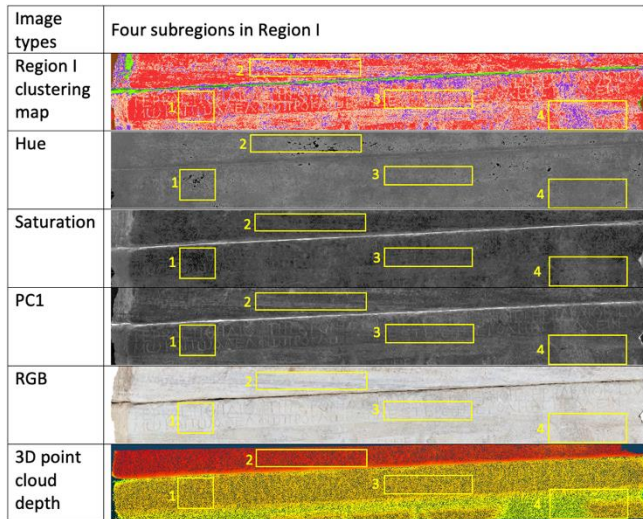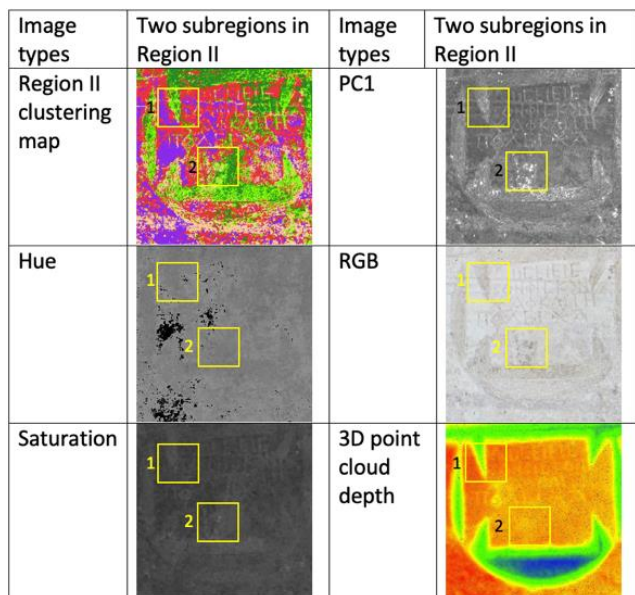

Figure 10. Subregions in Region I

Figure 11. Subregions in Region II

The subregions in the two regions were selected from areas with different surface characteristics. Various surface characteristics of the regions, such as degradation level, depth structure, and inscription content, are described in Table 5 and 6.

Table 5. Surface futures of subregions in Region I

Subregions on Region I			
1	**2**	**3**	**4**
Inscribed and partially eroded surface	Shallow eroded surface	Inscribed surface	Depth surface

Table 6. Surface futures of subregions in Region II

Subregions on Region II	
1	**2**
Depth and slightly eroded surface	Eroded surface

Figure 12 presents the histograms of the surfaces in Region I, while Figure 13 displays the histograms of the surfaces in Region II. When evaluating the discrimination capability by comparing the histogram distributions with the surface features, image types with high discrimination information are marked with a plus sign (+), and those with low discrimination ability are indicated with a minus sign (-) in the tables. It was observed that the histogram distribution can be either a multiple peak distribution or a homogeneous distribution, representing the differences in surface features. Based on this result, the clustering images' discrimination capability has been demonstrated as a robust technique for different surface features.

Figure 12. Histograms of subregions in Region I and their discrimination capability

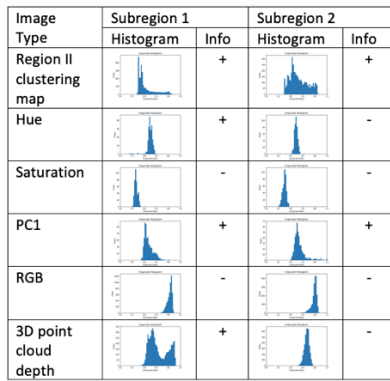| Image Type	Subregion 1		Subregion 2	
	Histogram	Info	Histogram	Info
Region II clustering map		+		+
Hue		+		-
Saturation		-		-
PC1		+		+
RGB		-		-
3D point cloud depth		+		-

Figure 13. Histograms of subregions in Region II and their discrimination capability

4. Discussion

In the applied methodology, orthophotos generated using photogrammetry are required first. The primary issue here is the low image resolution of multispectral cameras. The high resolution ratios between RGB and multispectral images pose a significant challenge for the georeferencing of the resulting orthophotos. This issue also impacts the effectiveness of the sharpening process applied afterward. Therefore, it is essential for the resolution ratios of the selected cameras to be as close to one another as possible. Ideally, this ratio should be near 1, indicating that the resolutions of the multispectral and RGB images should be identical. In this study, the ratio of multispectral to RGB resolution is 0.5. Based on this ratio, georeferencing and sharpening were successfully executed. Nominal values below 0.5 will likely lead to quality issues when creating an image stack.

The presence of common bands from both sensors in the image stack indicates the need for dimensional reduction. Another factor to consider regarding the cameras to be used is that multispectral ranges exhibit low overlap rates with one another, while the limited and extensive number of ultraviolet bands is anticipated to enhance the contribution of spectral analysis. Clearly, these cameras will enable the collection of more information from surfaces. The limited coverage of the multispectral sensor employed in this study can be seen as a disadvantage that diminishes performance during cluster analysis.

Searching for the optimal cluster number is crucial in the clustering study, as shown in Figures 4 and 5. Estimating the optimal number of clusters subjectively is challenging. Here, the optimal value is determined visually from the graph. It is also possible to automatically infer from the values presented in this graph using a differential numerical threshold value.

The classification method employed is based on an unsupervised learning approach. This comes with certain advantages and disadvantages when compared to supervised methods. The practical implementation of the algorithm and its rapid results can be viewed as positive aspects. However, the lack of reliance on training data inevitably weakens predictive power and hampers accurate accuracy analysis. Therefore, if feasible, a supervised learning algorithm utilizing surface samples in such a study will lead to the production of more stable and reliable information.

Finally, when we examine the surface maps, we find that some information about the surface can be identified. In particular, it is evident that the textual expressions on the sarcophagus are selectable, and the damaged areas on the surface of the sarcophagus can be detected. However, the expected performance is lacking in detecting the texts created by scraping. It is understood that the damaged surfaces, or the surface content differences, are detected more effectively than in the RGB image. The inability to sample the study surface due to its status as a historical artifact, along with the limitation of not being able to use a supervised algorithm, indicates that the resultant maps fall short in isolating some details.

The low-resolution characteristics of multi-spectral sensors are addressed with the new image enhancement method presented. However, no improvement could be made due to the bandwidths being insufficient for the analysis of the study. This deficiency can only be resolved by changing the sensor type. In this case, the information extraction capacity of the clustering produced is expected to increase. In future studies, it will be possible to evaluate the full effect by comparing sensors with different multispectral fields together.

5. Conclusion

In this study, a method for analyzing the surface features of cultural heritage artifacts using photogrammetry has been successfully developed. The proposed method can yield varying quality results depending on the sensor technology employed. Cameras with different bandwidths selected specifically for surface materials are anticipated to be more effective in this approach. Additionally, it is crucial for the high-resolution RGB camera to align with the resolution of the multispectral cameras to a certain degree. This alignment is vital for both geometric accuracy and radiometric quality. In future studies, comparing and evaluating different resolution ratios will help determine the optimum match.

This method is anticipated to provide valuable contributions through biochemical analysis on the surface, aiding both in the ground-truthing of data and in verifying information extracted from multispectral bands. This is also crucial for implementing trained classification.

Since two different regions on the surface were chosen for the study, these regions exhibited statistically similar radiometric properties. However, the primary reason for this situation can be attributed to the spatial proximity between the two regions. In other studies where this method will be applied, greater spatial distance may enhance regional differences. Therefore, conducting regional classifications on the surfaces is deemed more appropriate.

In future studies, in addition to orthophotos, which are photogrammetric products, utilizing another photogrammetric product, the point cloud, during classification may lead to improved results. On the other hand, because the historical artifacts are protected, permission issues prevent physical intervention, and they are considered outside the archaeological expertise,

sampling was not performed. However, obtaining more accurate results will be inevitable if sampling studies are conducted and chemical analyses of these samples are matched with the image.

Acknowledgement

Author contributions

Berna Pamuk: Data curation, Methodology, Software **Özgün Akçay:** Conceptualization, Programming, Validation, Writing-Reviewing and Editing.

Conflicts of interest

The authors declare no conflicts of interest.

References

1. Yakar, M., & Doğan, Y. (2017). Mersin Silifke Mezgit Kale Anıt Mezarı fotogrametrik rölöve alımı ve üç boyutlu modelleme çalışması. *Geomatik*, *2*(1), 11-17.
2. Zeybek, M., & Kaya, A. (2020). Tarihi Yığma Kiliselerde Hasarların Fotogrametrik Ölçme Tekniğiyle İncelenmesi: Artvin Tbeti Kilisesi Örneği. Geomatik, 5(1), 47-57. https://doi.org/10.29128/geomatik.568584
3. Bozdogan, O., Yaman, A., & Yılmaz, H. M. (2022). An analysis on the corrosion of a cultural heritage. International Journal of Engineering and Geosciences, 7(2), 112-127
4. Kasapakis, V., Gavalas, D., & Dzardanova, E. (2024). 3D Modelling Through Photogrammetry in Cultural Heritage. In Encyclopedia of Computer Graphics and Games, 23-26. Cham: Springer International Publishing.
5. Yakar, İ., Çelik, M. Ö., Hamal, S. N. G., & Bilgi, S. (2021). Kültürel mirasın dokümantasyonu çalışmalarında farklı yazılımların karşılaştırılması: Dikilitaş (Theodosius Obeliski) Örneği. Geomatik, 6(3), 217-226. DOI: 10.29128/geomatik.761475
6. Yakar, M., Uysal, M., Toprak, A. S., & Polat, N. (2013). 3D modeling of historical doger caravansaries by digital photogrammetry. *The International Archives of the Photogrammetry, Remote Sensing and Spatial Information Sciences*, *40*, 695-698.
7. Özdemir, E., Çallı, R., & Kartal, S. (2024). Utilization of unmanned aerial vehicles for the detection and localization of deteriorations in historical structures: a case study of Ishak Pasha Palace. International Journal of Engineering and Geosciences, 9(3), 377-389. https://doi.org/10.26833/ijeg.1464867
8. Mohammed, O., & Yakar, M. (2016). Yersel fotogrametrik yöntem ile ibadethanelerin modellenmesi. *Selcuk University Journal of Engineering Sciences*, *15*(2), 85-95..
9. Kanun, E., Alptekin, A., Karataş , L., & Yakar, M. (2022). The use of UAV photogrammetry in modeling ancient structures: A case study of "Kanytellis". Advanced UAV, 2(2), 41–50.
10. Çolak, A., Aktan, N., & Yılmaz, H. M. (2022). Modelling of its surroundings and Selime Cadhetral by UAV data. Advanced UAV, 2(1), 24–28.
11. Grifoni, E., Gargano, M., Melada, J., Interlenghi, M., Castiglioni, I., di Sturmeck, S. R. G., & Ludwig, N. (2022, April). Documenting Cultural Heritage in very hostile fruition contexts: the synoptic visualization of Giottesque frescoes by Multispectral and 3D Close-range Imaging. In Journal of Physics: Conference Series 2204(1), 012060. IOP Publishing.
12. Erdal, K., & Makineci, H. B. (2023). Adaptation analysis of produced 3D models from UAV-SLAM and UAV-TLS data combinations. Mersin Photogrammetry Journal, 5(1), 18-23. https://doi.org/10.53093/mephoj.1269630
13. Tuncer, S., & Avdan, U. (2024). Comparative analysis of non-invasive measurement methods for optimizing architectural documentation. International Journal of Engineering and Geosciences, 9(2), 302-313. https://doi.org/10.26833/ijeg.1424881
14. Fischnaller, F., Guidazzoli, A., Imboden, S., De Luca, D., Liguori, M. C., Russo, A., ... & De Lucia, M. A. (2015, September). Sarcophagus of the Spouses installation intersection across archaeology, 3D video mapping, holographic techniques combined with immersive narrative environments and scenography. In 2015 Digital Heritage, 1, 365-368. IEEE.
15. Unal, M., Yakar, M., & Yildiz, F. (2004, July). Discontinuity surface roughness measurement techniques and the evaluation of digital photogrammetric method. In Proceedings of the 20th international congress for photogrammetry and remote sensing, ISPRS (Vol. 1103, p. 1108).
16. Abdelmoniem, A. M., Mahmoud, N., Mohamed, W. S., Ewais, A. Y., & Abdrabou, A. (2020). Archaeometric study of a polychrome wooden coffin from 26th dynasty-Egypt. Mediterranean Archaeology and Archaeometry, 20(1), 7-7.
17. Yakar, M., & Doğan, Y. (2017). Mersin Silifke Mezgit Kale Anıt Mezarı fotogrametrik rölöve alımı ve üç boyutlu modelleme çalışması. *Geomatik*, *2*(1), 11-17.
18. Alberghina, M. F., Germinario, C., Bartolozzi, G., Bracci, S., Grifa, C., Izzo, F., ... & Lubritto, C. (2020). The Tomb of the Diver and the frescoed tombs in Paestum (southern Italy): New insights from a comparative archaeometric study. Plos One, 15(4), e0232375.
19. Frank, E., Heath, S., & Stein, C. (2021). Integration of photogrammetry, reflectance transformation imaging (RTI), and multiband imaging (MBI) for visualization, documentation, and analysis of archaeological and related materials. ISAW Papers.
20. Yilmaz, H. M., Yakar, M., & Yildiz, F. (2008). Digital photogrammetry in obtaining of 3D model data of irregular small objects. *The International Archives of the Photogrammetry, Remote Sensing and Spatial Information Sciences*, *37*, 125-130..
21. S Del Pozo, S., Rodríguez-Gonzálvez, P., Sánchez-Aparicio, L. J., Muñoz-Nieto, A., Hernández-López, D., Felipe-García, B., & González-Aguilera, D. (2017). Multispectral imaging in cultural heritage conservation. The International Archives of the Photogrammetry, Remote Sensing and Spatial Information Sciences, 42, 155-162.

22. Zainuddin, K., Majid, Z., Ariff, M. F. M., Idris, K. M., Abbas, M. A., & Darwin, N. (2019). 3D modeling for rock art documentation using lightweight multispectral camera. The International Archives of the Photogrammetry, Remote Sensing and Spatial Information Sciences, 42, 787-793.

23. Mandelli, A., Gobeil, C., Greco, C., & Rossi, C. (2021). Digital twin and 3d documentation of a Theban tomb at Deir Al-Medina (Egypt) using a multi-lenses photogrammetric approach. The International Archives of the Photogrammetry, Remote Sensing and Spatial Information Sciences, 43, 591-597.

24. Del Pozo, S., Herrero-Pascual, J., Felipe-García, B., Hernández-López, D., Rodríguez-Gonzálvez, P., & González-Aguilera, D. (2016). Multispectral radiometric analysis of façades to detect pathologies from active and passive remote sensing. Remote Sensing, 8(1), 80.

25. Yaman, H., & Özhan, T. (2021). A Roman Sarcophagus Depicting Scylla in the Çanakkale Troia Museum. Tekmeria, 16, 209-244.

26. McCann, A. M. (1978). Roman sarcophagi in the Metropolitan Museum of Art. Metropolitan museum of art.

27. Baş, G., & Yaman, A. (2022). 3D modeling of historical artifacts with terrestrial photogrammetric method: Roman sarcophagus and tomb stele example. Cultural Heritage and Science, 3(1), 12-18.

28. Yakar, M., Yildiz, F., Alyilmaz, C., & Yilmaz, H. M. (2009). Photogrammetric study for Sircali Medrese Door. In *9-th International Multidisciplinary Scientific GeoConference SGEM 2009* (pp. 879-884)..

29. Akçay, A., & Gürel, B. The contributions of computational imaging methods in archaeology: A case study in Termessos (Turkey), https://www.vi-mm.eu/wp-content/uploads/2018/11/A.Akcay-B.Gurel_A-Case-Study-In-Termessos-Turkey.pdf, Accessed 16 Mar 2024.

30. Ugolotti, G., Collina, F., Zambruno, S., Cornaglia, M., Iannucci, A., & Urcia, A. (2022). The 3D recording of the so-called Spreti sarcophagus in the Basilica of San Vitale (Ravenna, Italy). Digital Scholarship in the Humanities, 37(4), 1281-1288.

31. Browning Jr, D. C. (2024). Close-range photogrammetry for analysis of rock relief details: An investigation of symbols purported to be Jewish Menorahs in Rough Cilicia. Mersin Photogrammetry Journal, 6(1), 39-51. https://doi.org/10.53093/mephoj.1434605

32. Karataş, L., & Dal, M. (2023). Deterioration analysis of historical village house structure in Mersin Kanlıdivane archaeological area by UAV method. Mersin Photogrammetry Journal, 5(1), 32-41. https://doi.org/10.53093/mephoj.1290231

33. Kanun, E., Alptekin, A., Karataş, L., & Yakar, M. (2022). The use of UAV photogrammetry in modeling ancient structures: A case study of "Kanytellis". *Advanced UAV*, *2*(2), 41-50.

34. Laben, C. A., & Brower, B. V. (2000). US Patent No. 6,011,875. US Patent.

35. Ringnér, M. What is principal component analysis?, Nature biotechnology, 26 (3) (2008) 303–304.

36. Ikotun, A. M., Ezugwu, A. E., Abualigah, L., Abuhaija, B., & Heming, J. (2023). K-means clustering algorithms: A comprehensive review, variants analysis, and advances in the era of big data. Information Sciences, 622, 178-210. https://doi.org/10.1016/j.ins.2022.11.139.